IEEE Access
Multidisciplinary | Rapid Review | Open Access Journal

Received February 8, 2020, accepted February 17, 2020, date of publication February 28, 2020, date of current version March 11, 2020.

Digital Object Identifier 10.1109/ACCESS.2020.2977096

Removing Ring Artefacts for Photon-Counting Detectors Using Neural Networks in Different Domains

WEI FANG, LIANG LI, (Senior Member, IEEE), AND ZHIQIANG CHEN

Department of Engineering Physics, Tsinghua University, Beijing 100084, China
Key Laboratory of Particle and Radiation Imaging, Ministry of Education, Tsinghua University, Beijing 100084, China

Corresponding author: Liang Li (lliang@tsinghua.edu.cn)

This work was supported in part by the National Key Research and Development Program of China under Grant 2017YFC0109103, and in part by the NSFC under Grant 11775124 and Grant 11525521.

ABSTRACT The development of energy-resolving photon-counting detectors provides a new approach for obtaining spectral information in computed tomography. However, the responses of different photon counting detector pixels can be inconsistent, which will always cause stripe artefacts in projection domain and concentric ring artefacts in image domain. Traditional ring artifacts processing methods are mostly based on averaging and filtering. In this paper, we propose to use deep learning methods for ring artifacts removal respectively in image domain, projection domain and the polar coordinate system. Besides, by incorporating reconstruction process into neural networks, we unite the information from image domain and projection domain for ring artifacts removal under the framework of deep learning for the first time. A traditional ring artifacts removal method, which is based on wavelet and Fourier transform, is implemented for comparison. Quantitative analysis is performed on simulation and experimental results and it shows that deep learning based methods are promising in solving the problem of non-uniformity correction for photon-counting detectors.

INDEX TERMS Ring artefacts removal, deep learning methods, photon counting detectors, spectral CT.

I. INTRODUCTION

Photon counting detectors (PCDs) are attracting more and more attention in the next generation design of computed tomography systems [1]–[3]. Commercial products equipped with photon counting detectors for mammography have already been available and prototypes of computed tomography have also been demonstrated [4]–[8]. Energy discriminating photon counting detectors can resolve the energy information of incident X-ray photons by separating the resulting voltage pulses into multiple energy bins according to the pulse height, which is roughly proportional to the photon energy. Compared to energy integrating detectors (EIDs), photon counting detectors have following advantages: (a) the electronic noise and low energy scattering photons can be effectively eliminated in photon counting detectors by setting a suitable low-energy threshold, which will greatly improve the signal to noise ratio (SNR); (b) the contrast to noise ratio (CNR) and dose efficiency can also be improved by applying optimal energy weighting functions, such as assigning a higher weight to low-energy photons for their carrying more attenuation information [4]; and (c) with the ability of acquiring the spectral information, images in multiple energy windows can be generated with one-shot spectral imaging using photon counting detectors (PCDs), enabling more efficient quantitative material identification [9]–[11]. Therefore, photon counting spectral CT can be a great competitor to the existing energy-resolving techniques such as dual source CT, rapid kVp switching and differential beam filtering [12]; (d) beam hardening artifacts can also be alleviated by using spectral information obtained by photon counting detectors [5].

In general, photon counting detectors (PCDs) have a promising potential to offer significant improvements to the existing CT imaging techniques and make completely new CT applications possible. However, challenges still remain for its clinical applications. One of the most common defects of photon counting detectors is the inconsistence between the detector pixels, which will lead to stripe artefacts in projection data and consequently cause concentric ring artefacts in

The associate editor coordinating the review of this manuscript and approving it for publication was Hengyong Yu.

reconstructed images. This kind of inconsistence can have many causes: (a) some individual detector pixels can be defective, whose values are close to zero or saturated in projection domain; (b) insufficient detector calibration can also cause inconsistence between different detector pixels; (c) x-ray source structural patterns and changes of temperature conditions over time are also possible reasons for this kind of non-uniformity of detector sensitivity [13].

Due to the complex causes of detector sensitivity inconsistence and its relevance with the scanning object, it is still a challenging problem to reduce ring artefacts without impairing the image quality. Existing ring artefacts reduction techniques can be generally divided into two groups: pre-processing methods and post-processing methods. Pre-processing methods are performed in projection domain. In projection domain, the non-uniformity artefacts manifest as stripes, which are relatively easy to detect and eliminate compared to concentric rings in image domain. A common method for pre-processing in projection domain is known as flat-field correction [14]. However, it is still difficult to totally eliminate all the artefacts solely through using flat-field correction because it doesn't take the incident spectrum and the scanned object into consideration. Besides flat-field correction, hardware based approaches like moveable detector array [15] and dual gain calibration technique [16] were also proposed for non-uniformity correction. Getzin *et al.* proposed a first and second moment correction method based on the measured data for photon-counting detectors. Considering the special morphological structure of the stripe artefacts in projection domain, many inconsistence correction methods based on filtering have been raised by different researchers [17]–[23].

Post-processing methods are based on image domain. They directly deal with the reconstructed images because raw projection data is not always available. Since ring artefacts manifest as stripes after polar transform, many post-processing methods are performed in polar coordinate system. Sijbers and Postnov proposed a filtering method with a sliding window in the polar coordinate system [24]. Prell *et al.* compared mean and median filtering respectively in Cartesian coordinate and polar coordinate system and conclude that it is better to perform their algorithm in polar coordinate system [25]. Some iterative methods based on prior information were also put forward. Liang *et al.* proposed to use an iterative framework with relative total variation for ring artefacts removal [26]. Yan *et al.* proposed an variation-based ring artefacts removal method with sparse constraint [27]. Titarenko *et al.* proposed to use a two-stage method with a prior information on the attenuation coefficients for ring artefacts removal [28]. Wu *et al.* proposed a ring artefacts removal method based on TV-Stokes and unidirectional total variation model [29]. Salehjahromi *et al.* proposed an iterative reconstruction method with a directional total variation regularization term for ring artefacts removal [30]. However, most of these methods seem to oversimplify the problem or impose strong assumptions. And some iterative methods suffer from high computational cost. Also, the performance of these methods can be highly dependent on the extent and severity of the ring artefacts.

Recently, deep learning techniques have achieved great success in computer vision field [31]. Deep learning has also generated huge enthusiasm in the field of medical imaging. Deep learning techniques have been widely used for low dose CT denoising [32]–[34], metal artefacts suppression [35], [36] and spectral CT material decomposition [37]. Deep learning can also perform well on ring artefacts removal. Some initial results have been reported. Matthew Holbrook *et al.* proposed to use a convolutional neural network for removing stripe artefacts in projection data [38]. Chang *et al.* proposed a hybrid method which combines the advantages of deep learning and traditional methods for ring artefacts removal [39]. Wang *et al.* proposed a ring artifacts removal method for CBCT images by using a generative adversarial network with unidirectional relative total variation loss [40]. More work should be done in this direction. In this paper, we perform ring artefacts respectively in image domain, projection domain and polar coordinate system. Besides, by implementing image reconstruction process as a neural network module, it is for the first time that we unite the structural information in image domain and raw information in projection domain for ring artefacts removal under the framework of neural network training. The rest of this paper is organized as following. Section II describes the non-uniformity problem of photon-counting detector, the preparation of the training dataset, the architecture of the network and the training of the neural network using simulated data. Section III presents the testing simulation results and corresponding quantitative analysis. Section VI is about the results of applying the simulated-data-trained neural networks on the experimental data and quantitative evaluation is also presented. Section IV is the discussion and section V is the conclusion.

II. METHODS AND MATERIALS

A. PROBLEM STATEMENT

The cause of non-uniformity in photon-counting detector is complicated. Generally, the relationship between the incident and measured photon counts can be depicted like this [30]:

$$I_i = C_m I_0 \exp\left(-D_m \int_{ray_i} \mu dl\right), \tag{1}$$

where I_i and I_0 respectively represent the received and emitted photon counts. The integral represents the sum of the attenuation coefficients along the i_{th} ray. Two factors are introduced to depict the non-ideality in the detection process. The factor C_m represents the linear gain coefficient between the measured counts and the incident photon counts for the m_{th} detector pixel, which relates to the response function of the detector pixel. The factor D_m represents the gain factor caused by unwanted physical effects like beam hardening and scattering while the line-ray penetrating the scanned object. By performing some transformations, formula (1) can be

rewrittern as:

$$\int_{ray_i} \mu dl = -\left(\frac{1}{D_m}\right)\log\left(\frac{I_i}{I_0}\right) + \frac{\log(C_m)}{D_m}. \quad (2)$$

Then the relationship between the real projection data and the measured projection data for the m_{th} detector pixel can be illustrated as a linear model:

$$p^{\text{real}} = g_m \cdot p^{\text{measured}} + o_m. \quad (3)$$

The gain factor g_m and the shift o_m are decided by C_m and D_m in formula (2). We assumed that factors C_{m} and D_m are constants for the m_{th} detector pixel. So, the gain factor g_m and the offset o_m are also constants for the m_{th} detector pixel.

B. TRAINING DATA PREPARATION

It is difficult to acquire experimental training dataset including both ring artefacts corrupted images and corresponding clean images. So, it is necessary to simulate training dataset for network training. In this part, a CT image database including non-uniformity corrupted data and corresponding non-uniformity free data respectively in image domain, projection domain and polar coordinates is established. Clinical CT images of 10 patients from 2016 AAPM Low Dose CT Grand Challenge are used as artefacts free images. By performing forward projection, we can get the reference sinogram from the artefacts-free images. The non-uniformity we simulated is based on a realistic photon counting detector (eV3500, eV PRODUCTS, Saxonburg). To extract the feature of the detectors' non-uniformity, firstly we apply an iterative ring artefacts removal algorithm [41] to estimate the parameters of the non-uniformity for the photon counting detector. This iterative algorithm assumes that the relation between the real sinogram and the measured sinogram is a linear model as demonstrated in formula (3). The goal of the algorithm is to estimate the gain factor g and the offset o for each detector pixel. The algorithm assumes that the projection pixel values are spatially smooth while moving with respect to detectors. The local spatially neighbourhood average pixel values are used as the reference:

$$\min. \sum_n (g_m \cdot p_{n,m}^{\text{measured}} + o_m - p_{n,m}^{\text{average}})^2, \quad (4)$$

where n is the index of views, m is the index of detector pixels and $p_{n,m}^{\text{average}}$ is the mean value of the neighborhood pixels. By applying the gradient descent method, we can finally obtain the optimized gain factor g and offset o for each of the 256 detector pixels. We calculate the mean value and covariance for the overall 256 g and denote them as g_mean and g_cov. Similarly, we calculate the mean value and covariance for the overall 256 o and denote them as o_mean and o_cov. These four parameters indicate the statistical feature of the gain and the offset coefficients. Also, they reflect the severity of the inconsistence of the realistic detector pixels. These parameters are used to build two random variables to depict the distribution of gain and offset coefficients. Without loss of generality, we assume that they subject to Gaussian distributions:

$$G \sim N(g\_mean, g\_\text{cov}), \quad O \sim N(o\_mean, o\_\text{cov}). \quad (5)$$

With the above two Gaussian distributions, we can randomly generate many gain and offset coefficients g' and o'. These randomly generated coefficients are used to introduce variational non-uniformity to the original reference sinogram, which can be expressed as

$$p^{\text{simu}} = g' \cdot p^{\text{ref}} + o', \quad (6)$$

where p^{simu} and p^{ref} respectively represent the simulated non-uniformity corrupted projection data and the clean reference projection data measured by one certain detector pixel. It should be noted that g' and o' are different for each detector pixel and also different in different simulated sinograms. Fig. 1 demonstrates the process of training dataset establishment. After we get non-uniformity corrupted sinograms, we reconstruct them using FBP method to get ring artefacts corrupted images. We also perform Cartesian-Polar transform to the clean and corrupted reconstructed images and then we can get corresponding images in the polar coordinate system. In summary, after the whole training data preparation process, we get three pair of data sets including corrupted data and corresponding clean data respectively in image domain, projection domain and polar coordinate system. It is worth noting that the objective of this paper is not to obtain the most accurate photon counting detector response function. The non-uniformity simulation part can be simple and brief as long as it can help generate similar ring artefacts to the experimental ring artefacts. That's why a simple linear model can be used for generating ring artefacts. Actually, the simplicity of the training data preparation process to some extent exactly shows the flexibility of deep learning techniques on removing potential ring artefacts.

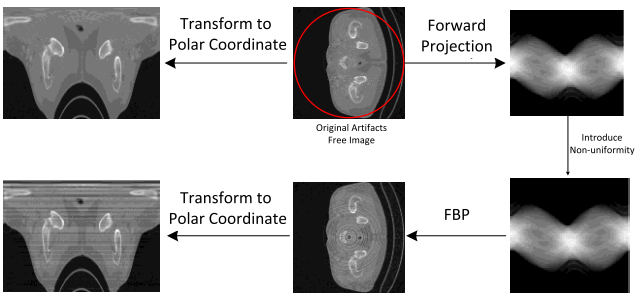

FIGURE 1. The process of training dataset establishment.

C. COORDINATE SYSTEM TRANSFORM

The details of Cartesian-Polar coordinate system transform are illustrated in this part. We denote the image in Cartesian coordinate system as $C(x, y)$, where x and y respectively represent the pixel index in width and height direction. And we denote the image in polar coordinate system as $I(\rho, \theta)$, where ρ and θ respectively represent radial distance and polar

angle. The pixel index in Cartesian coordinate system and polar coordinate system has a relation:

$$x = \rho\cos(\theta) + W/2, \quad y = \rho\sin(\theta) + H/2, \tag{7}$$

where W and H respectively represent the width and height of the image in Cartesian coordinate system. In our experiment, the image size in Cartesian coordinate system is [256, 256]. To minimize the resolution loss in the coordinate system transform, we set the radial sampling rate in polar coordinate system two times of the sampling rate in the Cartesian coordinate system. The sampling interval for polar angle is one degree. So, the size of transformed image in polar coordinate system is [256,360]. It should be noted that the region in the original image that is transformed to polar coordinate system is the inscribed circle, not the whole image, which is denoted as red circle in Fig. 1.

D. NETWORK STRUCTURE AND TRAINING

Fig. 2 illustrates the network we applied in image domain for ring artefacts removal. The input of the network is the corrupted image and the output of the network is the ring artefacts. After subtracting the estimated ring artefacts from the original corrupted image, we can get the artefacts free image. The main framework of the network is a modified 5-stage U-net [42]. The network has a contracting path and a symmetric expanding path, which are composed of convolution layers, batch normalization layers and rectified linear unit (ReLU) activations. The left part of the network is connected with max-pooling layers between stages and the right part of the network is connected with max-unpooling layers between stages. The left half of the network can be seemed as an encoding path and the right part of the network is a decoding path. For the convolution layer, the kernel size is 3×3 and the stride size is 1. Padding is added to keep the image size unchanged in the convolution layer. The number of feature channels is doubled after each pooling layer in the encoding path for better ring artefacts feature extracting.

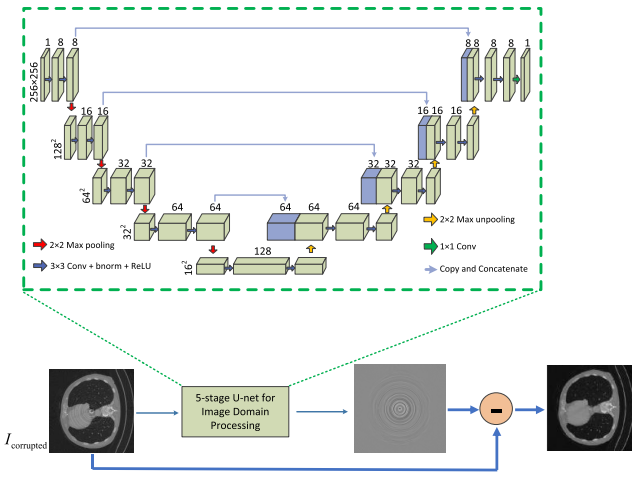

FIGURE 2. The architecture of ring artefacts removal network in image domain.

Vertically, the network has five stages, which are designed to process information in five different scales. The copying and concatenation process help recover the information lost in the down sampling process of the encoding path. And the pooling layers can help increase the effective receptive field of the network.

Fig. 3 illustrates the diagram of ring artefacts removal in projection domain. The input of the network is the corrupted projection data and the output is the estimated stripe artefacts of the projection data. The artefacts free projection data can be obtained by subtracting the stripe artefacts from the original corrupted projection data. After the subtraction, FBP algorithm is used for reconstruction. The architecture of the network for projection domain processing is the same with the modified U-net in Fig. 2 except for that the input image size is different. The input size of the projection domain network is [360, 601], which is the size of the input sinogram. In the projection simulation process, the number of views for forward projection is 360 and the number of detector pixels is 601.

Fig. 4 shows the diagram of ring artefacts removal in the polar coordinate system. Firstly, the original ring artefacts corrupted image is transformed to polar coordinate system. The red circle represents the region that is transformed to polar coordinates. The non-uniformity manifests as horizontal stripe artefacts in the transformed image. This image is then input to the network for stripe artefacts estimation. The network here is a modified 5-stage U-net, which has the same architecture with the image domain network. The output of the network is the estimated stripe artefacts. The artefacts free image can be obtained by getting the estimated stripe artefacts subtracted. After that, the image is transformed back to Cartesian coordinates.

The modified 5-stage U-structure networks in above three methods are all trained using stochastic gradient descent (SGD) method. The learning rate is set to 0.001 and the momentum is set to 0.9. The loss function for the network is mean square error (MSE) and the number of training epoch is 250. PyTorch is used for the network implementation. The computation is performed on a stand-alone work station equipped with a GTX 1080Ti graphic processor. Of all the simulated images, 4800 images from 8 patients are used for training dataset. 610 images and 526 images from another two patients are respectively used for validation and testing. The dataset of each patient includes around 600 slice images which range from chest to thigh.

E. THE COMPREHENSIVE MODEL

In the past, the non-uniformity correction method is either subject to pre-processing methods or post-processing methods. In other words, the method is performed either on projection data or on the reconstructed image. These two types of methods are isolated. In this paper, by incorporating the reconstruction process into the neural network, we can unite the image domain and projection domain processing

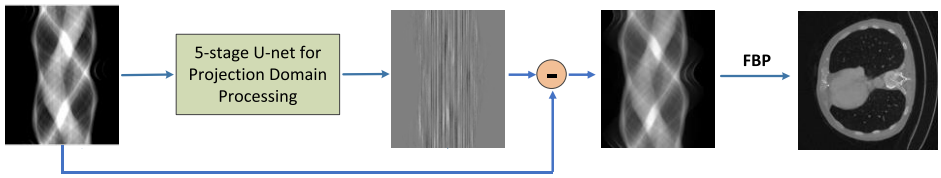

FIGURE 3. The diagram of ring artefacts removal in projection domain.

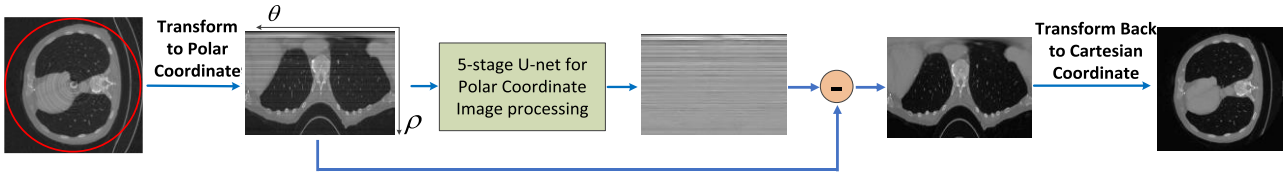

FIGURE 4. The diagram of ring artefacts removal in polar coordinate system.

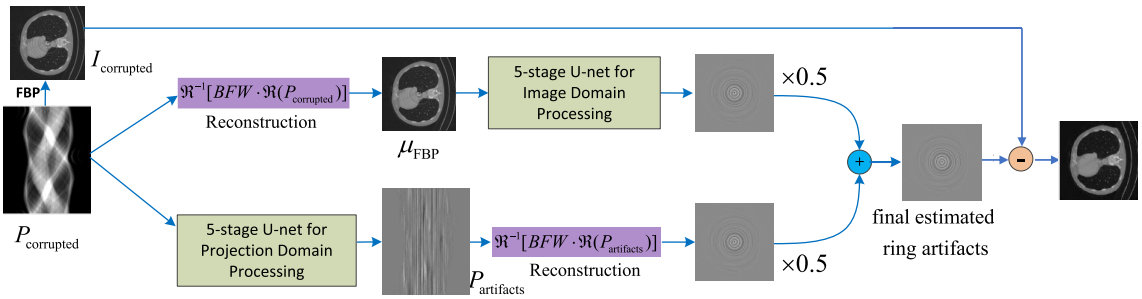

FIGURE 5. The diagram of ring artefacts removal using a comprehensive model.

for non-uniformity correction under the framework of deep learning.

The FBP reconstruction method can be performed in the form of matrix multiplying [43]:

$$\mu_{\text{FBP}} = \mathcal{R}^{-1}\left[BFW \cdot \mathcal{R}(p)\right], \tag{8}$$

where p represents the projection data and μ_{FBP} denotes the reconstructed image. $\mathcal{R}$ is an operator that reshapes projection data into a vector and $\mathcal{R}^{-1}$ is the corresponding inverse operator that reshapes the vector into the two-dimensional reconstructed image. The matrix W is used for weighting and F is for filtering. The matrix B performs back-projection to the filtered projection. This form of reconstruction, which is in the form of matrix multiplying, can be easily implemented in PyTorch by using its interface for sparse tensor. The operation behind this matrix multiplying form is the same with regular FBP reconstruction. Also, the three matrixes for reconstruction are fixed in the network training. The reconstruction process functions as a connection between the projection domain and image domain. Our comprehensive model has two branches, just as illustrated in Fig. 5. The first branch accepts corrupted projection data as input and then reconstructs it using formula (8). After that, the reconstructed image is input to a 5-stage U-net for image domain ring artefacts estimation. The architecture of this U-net is the same with the image domain network whose structure is illustrated in Fig. 2. The output of this 5-stage U-net is the estimated ring artefacts. The second branch also accepts the corrupted projection data as input. It is connected with a 5-stage U-net for projection domain stripe artefacts estimation. This projection-domain U-net is the same with the projection domain network in Fig. 3. The estimated stripe artefacts are reconstructed using (8) to get corresponding estimated ring artefacts. The estimated ring artefacts from the first and second branches are respectively multiplied with factor 0.5 and then added to get the final estimated ring artefacts. The final estimated ring artefacts are subtracted from the corrupted image and then we can get the final artefacts-free image.

It will be very time-consuming to train the model from the beginning because the model consists of image reconstruction process. The strategy we applied here is to use the models that we already trained for image domain processing and projection domain processing as the beginning state for the two sub-networks in the two branches. And then we can train the whole network for like 10 epochs. The advantage of the comprehensive model is that it can combine the raw information in projection domain and the structural information in image domain for non-uniformity correction. The simulation results show that the comprehensive model performs better

than the ring artefacts removal method that merely in image domain or projection domain.

F. TWO TRADITIONAL METHODS FOR COMPARISON

Two traditional ring artefacts removal methods are implemented for comparison. The method we choose is popular Wavelet-Fourier (WF) filtering method [17]. This method is based on combined wavelet and Fourier analysis and can eliminate horizontal and vertical stripes in images. We apply this method respectively in projection domain and polar coordinates as the artefacts in these two domains manifest as stripes. After we applying this WF method on projection data, the processed projection data is reconstructed to image domain for image quality evaluation. Similarly, the WF method processed data in polar coordinates is transformed back to Cartesian coordinates for image quality evaluation.

III. RESULTS ON SIMULATION DATA

A. SIMULATION RESULTS

According to the methods we have illustrated above, we have six methods for non-uniformity correction. And they are respectively WF method in projection domain, WF method in polar coordinates, U-net in image domain, U-net in projection domain, U-net in polar coordinates and the comprehensive model. Fig. 6 shows the two cases of the 526 testing dataset. And Fig. 7 shows the corresponding processed results and the error of these two cases by using these six methods.

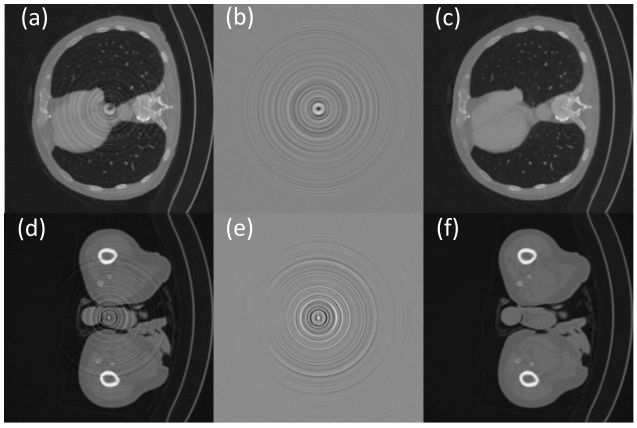

FIGURE 6. Two cases of testing data. (a) The simulated corrupted image. (b) The introduced ring artefacts. (c) The reference image. (d, e, f) are the corresponding images for the second case. The display window for the corrupted image and the reference image is [0,0.4]. The display window for the introduced ring artefacts is [−0.1,0.1].

We can see that the processed images of traditional WF methods remain a lot of low-frequency ring artefacts whether it is performed in projection domain or polar coordinate system. The filtering process in WF method does not completely remove artefacts but tends to change the severe high-frequency artefacts into smooth low-frequency ring artefacts. Compared to WF method, deep learning methods perform relatively better. The results obtained by different deep learning methods are all visually similar to standard images and almost indistinguishable. By judging from the error

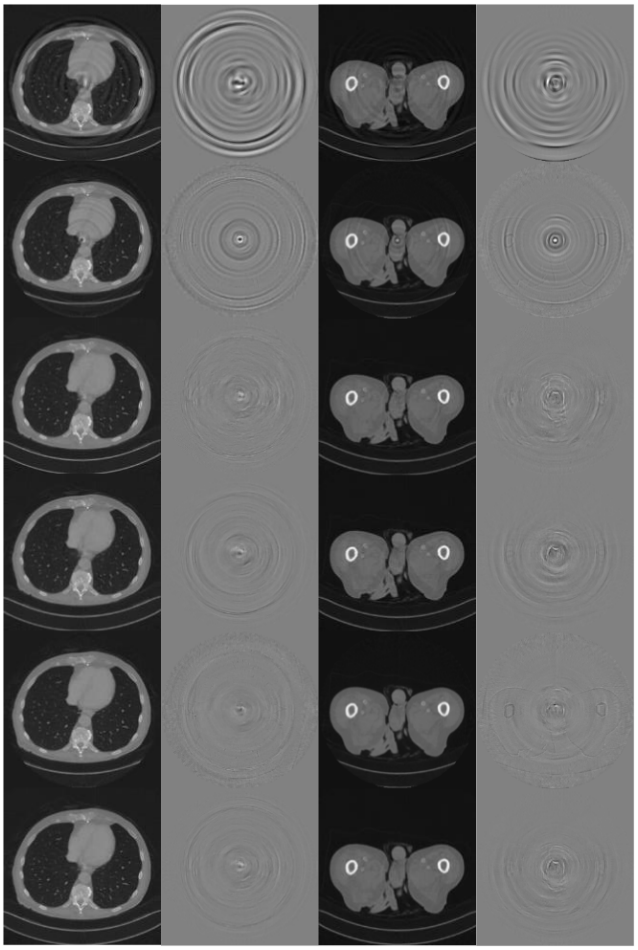

FIGURE 7. Images in the first and third column are the processed results. The images in the second and fourth column are corresponding error images of the six methods. From top to bottom, the methods are respectively WF method in projection domain, WF method in polar coordinates, U-net in image domain, U-net in projection domain, U-net in polar coordinates and the comprehensive model. The display window for the processed results is [0,0.4]. The display window for the error image is [−0.1, 0.1].

image, we can tell the slight difference between the deep learning methods that work respectively in image domain, projection domain, polar coordinates and the comprehensive model. There seems to be not too much difference between the results obtained by the U-net in image domain and projection domain. The network that works in polar coordinate system performs well in ring artefacts removal but seems to suffer from the resolution loss caused by the Cartesian-polar coordinate transform judging from the error image. The comprehensive model has the best performance after combining the structural information in image domain and the raw information in projection domain for ring artefacts removal. It is better than estimating artefacts merely in projection domain or image domain judging from the error image. This can be seen more clearly from the quantitative analysis below.

B. SIMULATION RESULTS EVALUATION

To quantitatively compare the above six methods, two indicators are chosen to evaluate the proposed network, including

the relative root of mean square error (RRMSE) and the structural similarity (SSIM) index. The original artefacts free image is used as the gold standard in the evaluation. The two indicators are defined as:

$$\text{RRMSE} = \frac{||\hat{\mu} - \mu||_2}{||\mu||_2}, \tag{9}$$

$$\text{SSIM} = \frac{(2\bar{\hat{\mu}}\bar{\mu} + C_1)(2\sigma_{\hat{\mu}\mu} + C_2)}{(\bar{\hat{\mu}}^2 + \bar{\mu}^2 + C_1)(\sigma_{\hat{\mu}}^2 + \sigma_{\mu}^2 + C_2)}, \tag{10}$$

where $\hat{\mu}$ represents the processed image and μ is the corresponding reference image. $\bar{\hat{\mu}}$ and $\bar{\mu}$ represent their mean values. $\sigma_{\hat{\mu}}$ and σ_{μ} represent the standard deviations of $\hat{\mu}$ and μ respectively. $\sigma_{\hat{\mu}\mu}$ represents the covariance between $\hat{\mu}$ and μ. We calculated the RRMSE and SSIM for each of the 526 images in the test set. The results are shown in Fig. 8 and Fig. 9. We also calculated the mean value and standard deviation of these RRMSE and SSIM achieved by these six methods for the whole test set, which are shown in Table 1.

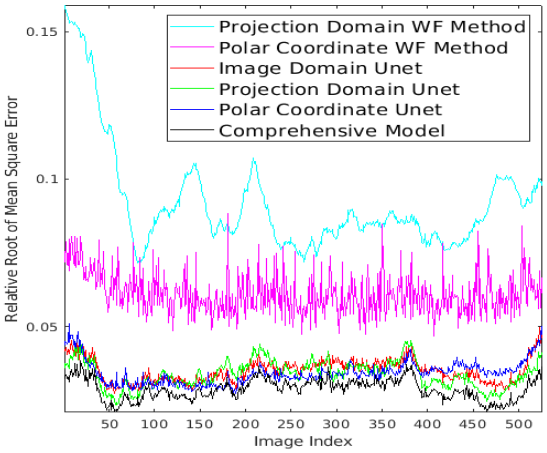

FIGURE 8. RRMSE achieved by the six methods on the testing dataset.

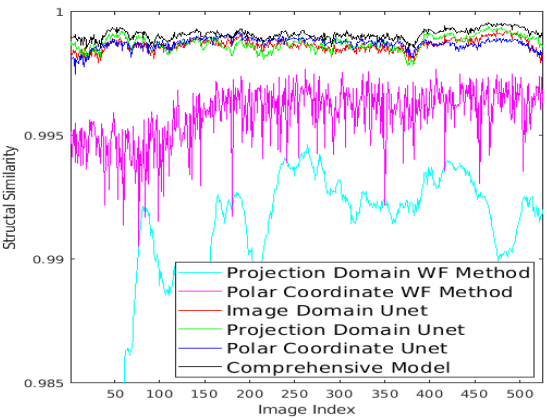

FIGURE 9. SSIM achieved by the six methods on the testing dataset.

We can clearly see that the four deep learning based methods get lower RRMSE and higher SSIM compared to traditional WF methods, which shows great power of deep learning methods for ring artefacts extraction. Among the four deep learning based methods, the comprehensive model achieves the lowest RRMSE and the highest SSIM after combining the information from both the image domain and projection domain. The standard deviation represents the stability of the method. We can conclude that the comprehensive model is also the most stable one.

TABLE 1. Means and Stds of RRMSE and SSIM over the testing dataset.

Methods	RRMSE	SSIM
Projection Domain WF	0.0921 ± 0.0181	0.99021 ± 0.00439
Polar Coordinate WF	0.0611 ± 0.0071	0.99582 ± 0.00116
Image Domain U-net	0.0351 ± 0.0039	0.99864 ± 0.00024
Projection Domain U-net	0.0339 ± 0.0046	0.99873 ± 0.00029
Polar Coordinate U-net	0.0342 ± 0.0040	0.99871 ± 0.00023
Comprehensive Model	$\mathbf{0.0288 \pm 0.0036}$	$\mathbf{0.99908 \pm 0.00020}$

IV. RESULTS ON EXPERIMENTAL DATA

A. EXPERIMENTAL DATA PREPARATION

We also applied the simulation-data-trained networks on the experimental datasets. The experimental projection data is acquired by using a linear-array CdZnTe photon counting detector (eV3500, eV PRODUCTS, Saxonburg, PA) which has 256 pixels with the size of each pixel being 0.5 mm $\times$ 2 mm. The x-ray source is a conventional benchtop x-ray tube (G-297, Varian). Table 2 shows the detailed operational condition of the experiment.

TABLE 2. Some operational parameters of the experiment.

Operational parameters	Value
X-ray tube voltage	80kV
X-ray tube current	20uA
Distance between tube and detector	70.4cm
Distance between object and detector	31.96cm
Number of projections	360
The exposure time per angle	5s

The scanned object is a mouse in a cylindrical container. Animal experiments were approved by the Laboratory Animal Research Centre of Tsinghua University (Animal Protocol (AP) code: 17-LL1, AP date:27/09/2017-27/09/2020). Before network processing, experimental dataset undergoes a linear mapping to get aligned with the simulation dataset in respect of mean value and covariance. The experimental images are back-mapped to the original value level after the network processing.

B. EXPERIMENTAL RESULTS

Fig. 10 shows the performance of different ring artefacts removal methods on the above four experimental cases. The first row shows the four original reconstructed images. We can see that the images are severely corrupted by the

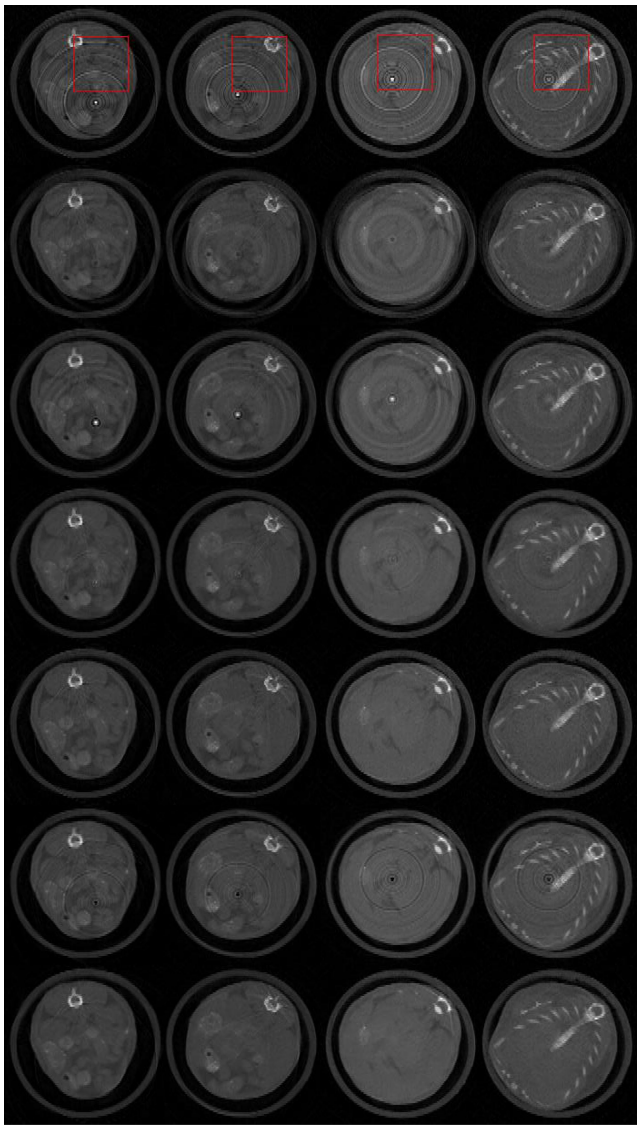

FIGURE 10. The comparison of different ring artefacts removal methods on experimental dataset. Each row is the corresponding results obtained by a certain method. From top to bottom, the results are respectively the original images, the processed images of WF method in projection domain, WF method in polar coordinates, U-net in image domain, U-net in projection domain, U-net in polar coordinates and the comprehensive model. The display window is [0, 0.46].

ring artefacts due to the detector non-uniformity. The red rectangle shows the area we chose for quantitative analysis later. The second and third rows show the results obtained by traditional Wavelet and Fourier (WF) filtering method respectively in projection domain and polar coordinate system. We can see that the results still remain a lot of low-frequency ring artefacts after processing whether the WF method is performed in projection domain or polar coordinate system. The reason for that may be the ring artefacts caused by the non-uniformity of photon-counting detectors are so heavy that it is difficult for this kind of filtering-based method to handle. We have also seen a similar situation in the above simulation results. Compared to WF methods, deep learning based methods have better performance on experimental dataset. The fourth row shows the results obtained by the image domain network. We can see that the image domain network can remove most ring artefacts from the original image, but there are still some slight ring artefacts left in the processed images. The sixth row is the results obtained by using deep learning methods in polar coordinate system. We can find that extracting stripe artefacts in polar coordinates performs not so well on the experimental dataset since many small ring artefacts are still left in the processed image. Besides, the results obtained by the polar coordinate network tend to have a small dark point at the centre of the image. We think this may be caused by the coordinates transform. The central point in the Cartesian coordinate system is corresponding to a line in the polar coordinate system. So, a slight error in this line after network processing will finally accumulate at the central point after transforming back to Cartesian coordinate system. The fifth row and the seventh row are respectively the results of projection domain network and the comprehensive model. We can figure out that the projection domain network and the comprehensive model both perform impressively well on the experimental dataset. For the comprehensive model, it combines the advantages of the projection domain network and the image domain network. The projection domain network part can effectively remove most ring artefacts while the image domain network part in the comprehensive model can help supress some small artefacts and noise in the original image to make the image clearer, which can be especially seen in the fourth case.

C. EXPERIMENTAL RESULTS EVALUATION

The experimental results are also quantitatively evaluated to compare these different ring artefacts removal methods. Since we do not have reference images like in simulation dataset for the experimental dataset. Two other indicators were used for evaluation. The first one is line-ratio, which is inspired by a recent non-uniformity correction work [44]. The line-ratio is calculated in projection domain, so we firstly performed forward projection on the processed results to obtain the corresponding projection data according to the original reconstruction geometry. And then we calculate the line-ratio for each detector pixel in the projection domain. The line-ratio can be defined as:

$$ratio_m = \sum_{n=1}^{N} \frac{p_{n,m-1} + p_{n,m+1}}{2p_{n,m} \cdot N}, \tag{11}$$

where p represents the projection data and N is the number of view angles. The notation n and m respectively represent the angle index and detector pixel index of the projection data. For an image free of ring artefacts, the generated corresponding projection data will also be free of stripe artefacts and its line-ratio values will all approximate one. For an image corrupted by ring artefacts, its corresponding projection data will have a lot of stripe artefacts and the calculated line-ratio values will have strong fluctuations around one. Fig. 11 shows the calculated line-ratio values of the processed experimental results obtained by different methods. We can see that the

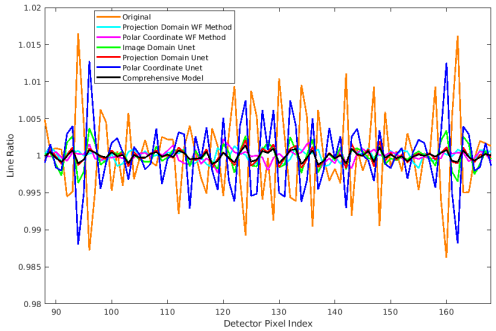

FIGURE 11. The line-ratios of experimental results for different ring artefacts removal methods.

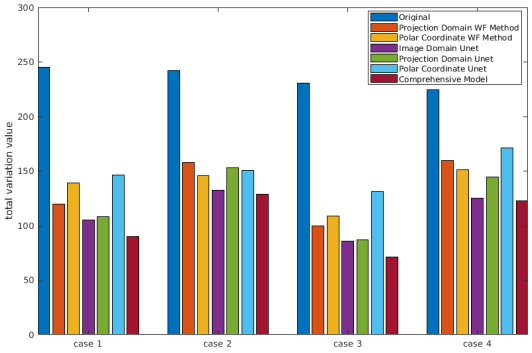

FIGURE 12. The total variation of the processed results by using different methods.

line-ratios for the original image (orange line) go up and down around one, indicating the strong non-uniformity between detector pixels. While the calculated line-ratio values of the results obtained by the projection domain U-net method (red one) and the comprehensive model method (black one) are much smoother, which means almost no ring artefacts are left in the processed images.

Table 3 lists the standard deviations of the above line-ratios. We can see that the line-ratio of the comprehensive model is the smoothest one with the smallest standard deviation value, which indicates the comprehensive model achieves the best performance on ring artefacts removal.

TABLE 3. Standard deviations of line-ratios of experimental results.

Methods	Standard deviations ($\times 10^{-4}$)
Original	60.1
Projection Domain WF	7.8
Polar Coordinate WF	8.4
Image Domain U-net	15.2
Projection Domain U-net	8.8
Polar Coordinate U-net	44.7
Comprehensive Model	**6.0**

To further compare the performance of ring artefacts removal and noise suppression for different methods, we also calculated the total variation of the four rectangle regions in Fig. 10. The definition of total variation is as following:

$$TV = \sum_{i,j} |x_{i,j} - x_{i-1,j}| + |x_{i,j} - x_{i+1,j}| + |x_{i,j} - x_{i,j-1}| + |x_{i,j} - x_{i,j+1}|, \quad (12)$$

where x represents the reconstructed image. The notation i and j are the vertical and horizontal index of the image pixels. The calculated total variation values of the four experimental cases are shown in Fig. 12.

We can see that the comprehensive model achieves the lowest total variation value after combining the advantages of both projection domain network processing and image domain network processing. It is noteworthy that though the image quality of the results obtained by projection domain network is visually good, its total variation value is not very low. On the contrary, the total variation value of the results obtained by image domain network is relatively low though some slight rings are still left in the processed images. We think the reason is that the convolution layer in the image domain U-net has a tendency to smoothen the image and suppress the noise, which leads to a lower total variation value. The image quality evaluation is performed in image domain. While the projection domain U-net is performed on projection data and cannot guarantee a smoothness in image domain.

V. DISCUSSION

The direct applying of the linear model [41] for ring artefacts correction performs not so well. Fig. 13 shows the obtained results of the four experimental cases by using the linear model. The algorithm seems to just performs a low-pass filtering to the images. We think the reason is that the algorithm estimates the gain and offset for each detector by assuming that the neighbouring pixel values in the sinogram are similar, which may be not true when the ring artefacts are very strong and bulky. But we think that the model is feasible for ring artefacts generation as long as it can help generate ring artefacts which are similar to the artefacts in experimental data. Besides, we think that the simplicity of the ring artefacts simulation exactly demonstrates the flexibility of deep learning methods on removing potential ring artefacts which may not be covered in simulation.

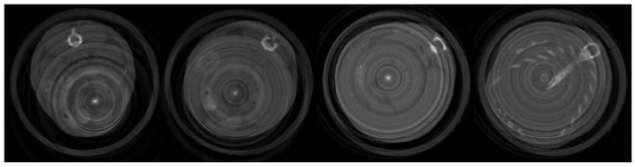

FIGURE 13. The experimental results of applying estimated gain and offset for ring artefacts correction. The original images are at the first row in Fig. 10.

VI. CONCLUSION

In this paper, we propose to use deep learning methods for ring artefacts removal respectively in image domain, projection domain and polar coordinate system. We also put

forward a comprehensive model for ring artefacts removal. By incorporating reconstruction process into neural networks, the comprehensive model combines the information from image domain and projection domain for ring artefacts removal under the framework of deep learning. A traditional stripe artefacts removal method, which is based on wavelet and Fourier transform, is implemented for comparison. Quantitative analysis is performed on the simulation results and it shows that deep learning based methods are promising in solving the problem of non-uniformity correction for photon-counting detectors. We also test the simulation-data-trained networks on the experimental dataset. The experimental results show that the projection domain network and the comprehensive model have a great performance on experimental ring artefacts removal for photon-counting detectors.

REFERENCES

[1] K. Taguchi and J. S. Iwanczyk, "Vision 20/20: Single photon counting X-ray detectors in medical imaging," *Med. Phys.*, vol. 40, no. 10, Sep. 2013, Art. no. 100901.

[2] H. Bornefalk and M. Danielsson, "Photon-counting spectral computed tomography using silicon strip detectors: A feasibility study," *Phys. Med. Biol.*, vol. 55, no. 7, pp. 1999–2022, Mar. 2010.

[3] P. M. Shikhaliev, "Energy-resolved computed tomography: First experimental results," *Phys. Med. Biol.*, vol. 53, no. 20, pp. 5595–5613, Sep. 2008.

[4] J. Berglund, H. Johansson, M. Lundqvist, B. Cederström, and E. Fredenberg, "Energy weighting improves dose efficiency in clinical practice: Implementation on a spectral photon-counting mammography system," *J. Med. Imag.*, vol. 1, no. 3, Aug. 2014, Art. no. 031003.

[5] J. P. Schlomka, E. Roessl, R. Dorscheid, S. Dill, G. Martens, T. Istel, C. Bäumer, C. Herrmann, R. Steadman, G. Zeitler, A. Livne, and R. Proksa, "Experimental feasibility of multi-energy photon-counting K-edge imaging in pre-clinical computed tomography," *Phys. Med. Biol.*, vol. 53, no. 15, pp. 4031–4047, Jul. 2008.

[6] M. Persson, B. Huber, S. Karlsson, X. Liu, H. Chen, C. Xu, M. Yveborg, H. Bornefalk, and M. Danielsson, "Energy-resolved CT imaging with a photon-counting silicon-strip detector," *Phys. Med. Biol.*, vol. 59, no. 22, pp. 6709–6727, Oct. 2014.

[7] Z. Yu, S. Leng, S. M. Jorgensen, Z. Li, R. Gutjahr, B. Chen, A. F. Halaweish, S. Kappler, L. Yu, E. L. Ritman, and C. H. McCollough, "Evaluation of conventional imaging performance in a research whole-body CT system with a photon-counting detector array," *Phys. Med. Biol.*, vol. 61, no. 4, pp. 1572–1595, Feb. 2016.

[8] J. P. Ronaldson, R. Zainon, N. J. A. Scott, S. P. Gieseg, A. P. Butler, P. H. Butler, and N. G. Anderson, "Toward quantifying the composition of soft tissues by spectral CT with Medipix3," *Med. Phys.*, vol. 39, no. 11, pp. 6847–6857, Oct. 2012.

[9] Y. Yao, L. Li, and Z. Chen, "Dynamic-dual-energy spectral CT for improving multi-material decomposition in image-domain," *Phys. Med. Biol.*, vol. 64, no. 13, Jul. 2019, Art. no. 135006.

[10] L. Li, Z. Chen, W. Cong, and G. Wang, "Spectral CT modeling and reconstruction with hybrid detectors in dynamic-threshold-based counting and integrating modes," *IEEE Trans. Med. Imag.*, vol. 34, no. 3, pp. 716–728, Mar. 2015.

[11] L. Li, Z. Chen, G. Wang, J. Chu, and H. Gao, "A tensor PRISM algorithm for multi-energy CT reconstruction and comparative studies," *J. X-Ray Sci. Technol.*, vol. 22, no. 2, pp. 147–163, 2014.

[12] T. Johnson, C. Fink, S. O. Schönberg, and M. F. Reiser, *Dual Energy CT in Clinical Practice*. Berlin, Germany: Springer, 2011.

[13] H. Bornefalk, M. Persson, C. Xu, S. Karlsson, C. Svensson, and M. Danielsson, "Effect of temperature variation on the energy response of a photon counting silicon CT detector," *IEEE Trans. Nucl. Sci.*, vol. 60, no. 2, pp. 1442–1449, Apr. 2013.

[14] J. A. Seibert, J. M. Boone, and K. K. Lindfors, "Flat-field correction technique for digital detectors," *Proc. SPIE*, vol. 3336, Jul. 1998, pp. 348–355.

[15] Y. Zhu, M. Zhao, H. Li, and P. Zhang, "Micro-CT artifacts reduction based on detector random shifting and fast data inpainting," *Med. Phys.*, vol. 40, no. 3, Feb. 2013, Art. no. 031114.

[16] P. G. Roos, R. E. Colbeth, I. Mollov, P. Munro, J. Pavkovich, E. J. Seppi, E. G. Shapiro, C. A. Tognina, G. F. Virshup, J. M. Yu, G. Zentai, W. Kaissl, E. Matsinos, J. Richters, and H. Riem, "Multiple-gain-ranging readout method to extend the dynamic range of amorphous silicon flat-panel imagers," *Proc. SPIE*, vol. 5368, May 2004, pp. 139–150.

[17] B. Münch, P. Trtik, F. Marone, and M. Stampanoni, "Stripe and ring artifact removal with combined wavelet—Fourier filtering," *Opt. Express*, vol. 17, no. 10, pp. 8567–8591, May 2009.

[18] M. Boin and A. Haibel, "Compensation of ring artefacts in synchrotron tomographic images," *Opt. Express*, vol. 14, no. 25, pp. 12071–12075, 2006.

[19] X. Tang, R. Ning, R. Yu, and D. Conover, "Cone beam volume CT image artifacts caused by defective cells in X-ray flat panel imagers and the artifact removal using a wavelet-analysis-based algorithm," *Med. Phys.*, vol. 28, no. 5, pp. 812–825, May 2001.

[20] F. Sadi, S. Y. Lee, and M. K. Hasan, "Removal of ring artifacts in computed tomographic imaging using iterative center weighted median filter," *Comput. Biol. Med.*, vol. 40, no. 1, pp. 109–118, Jan. 2010.

[21] E. M. A. Anas, S. Y. Lee, and M. K. Hasan, "Removal of ring artifacts in CT imaging through detection and correction of stripes in the sinogram," *Phys. Med. Biol.*, vol. 55, no. 22, pp. 6911–6930, Nov. 2010.

[22] M. Eldib, M. Hegazy, Y. Mun, M. Cho, M. Cho, and S. Lee, "A ring artifact correction method: Validation by micro-CT imaging with flat-panel detectors and a 2D photon-counting detector," *Sensors*, vol. 17, no. 2, p. 269, Jan. 2017.

[23] A. N. M. Ashrafuzzaman, S. Y. Lee, and M. K. Hasan, "A self-adaptive approach for the detection and correction of stripes in the sinogram: Suppression of ring artifacts in CT imaging," *EURASIP J. Adv. Signal Process.*, vol. 2011, no. 1, pp. 1–13, Aug. 2010.

[24] J. Sijbers and A. Postnov, "Reduction of ring artefacts in high resolution micro-CT reconstructions," *Phys. Med. Biol.*, vol. 49, no. 14, pp. N247–N253, Jul. 2004.

[25] D. Prell, Y. Kyriakou, and W. A. Kalender, "Comparison of ring artifact correction methods for flat-detector CT," *Phys. Med. Biol.*, vol. 54, no. 12, pp. 3881–3895, Jun. 2009.

[26] X. Liang, Z. Zhang, T. Niu, S. Yu, S. Wu, Z. Li, H. Zhang, and Y. Xie, "Iterative image-domain ring artifact removal in cone-beam CT," *Phys. Med. Biol.*, vol. 62, no. 13, pp. 5276–5292, Jun. 2017.

[27] L. Yan, T. Wu, S. Zhong, and Q. Zhang, "A variation-based ring artifact correction method with sparse constraint for flat-detector CT," *Phys. Med. Biol.*, vol. 61, no. 3, pp. 1278–1292, Jan. 2016.

[28] S. Titarenko, V. Titarenko, A. Kyrieleis, and P. J. Withers, "A ring artifact suppression algorithm based on *a priori* information," *Appl. Phys. Lett.*, vol. 95, no. 7, Aug. 2009, Art. no. 071113.

[29] H. Wu, J. Li, and H. Wang, "Removing ring artifacts in cone-beam CT via TV-Stokes and unidirectional total variation model," *Med. Phys.*, vol. 46, no. 4, pp. 1719–1727, Feb. 2019.

[30] M. Salehjahromi, Q. Wang, L. A. Gjesteby, D. Harrison, G. Wang, and H. Yu, "A directional TV based ring artifact reduction method," *Proc. SPIE*, vol. 10948, Mar. 2019, Art. no. 109482.

[31] Y. LeCun, Y. Bengio, and G. Hinton, "Deep learning," *Nature*, vol. 521, pp. 436–444, May 2015.

[32] H. Chen, Y. Zhang, W. Zhang, P. Liao, K. Li, and J. Zhou, "Low-dose CT via convolutional neural network," *Biomed. Opt. Express*, vol. 8, pp. 679–694, Feb. 2017.

[33] Q. Yang, P. Yan, Y. Zhang, H. Yu, Y. Shi, X. Mou, M. K. Kalra, Y. Zhang, L. Sun, and G. Wang, "Low-dose CT image denoising using a generative adversarial network with wasserstein distance and perceptual loss," *IEEE Trans. Med. Imag.*, vol. 37, no. 6, pp. 1348–1357, Jun. 2018.

[34] E. Kang, J. Min, and J. C. Ye, "A deep convolutional neural network using directional wavelets for low-dose X-ray CT reconstruction," *Med. Phys.*, vol. 44, no. 10, pp. e360–e375, Oct. 2017.

[35] Y. Zhang and H. Yu, "Convolutional neural network based metal artifact reduction in X-ray computed tomography," *IEEE Trans. Med. Imag.*, vol. 37, no. 6, pp. 1370–1381, Jun. 2018.

[36] C. Zhang and Y. Xing, "CT artifact reduction via U-net CNN," *Proc. SPIE*, vol. 10574, Mar. 2018, Art. no. 105741R.

[37] Z. Chen and L. Li, "Robust multimaterial decomposition of spectral CT using convolutional neural networks," *Opt. Eng.*, vol. 58, Jan. 2019, Art. no. 013104.

[38] D. P. C. M. Holbrook and T. C. Badea, "Ring reduction for micro CT using deep residual learning," in *Proc. 5th Int. Conf. Image Formation X-Ray Comput. Tomogr.*, Salt Lake City, UT, USA, 2018, pp. 415–418.
[39] S. Chang, X. Chen, J. Duan, and X. Mou, "A hybrid ring artifact reduction algorithm based on CNN in CT images," *Proc. SPIE*, vol. 11072, May 2019, Art. no. 1107226.
[40] Z. Wang, J. Li, and M. Enoh, "Removing ring artifacts in CBCT images via generative adversarial networks with unidirectional relative total variation loss," *Neural Comput. Appl.*, vol. 31, no. 9, pp. 5147–5158, Jan. 2019.
[41] D. A. Scribner, K. A. Sarkady, M. R. Kruer, J. T. Caulfield, J. D. Hunt, and C. Herman, "Adaptive nonuniformity correction for IR focal-plane arrays using neural networks," in *Proc. Infr. Sensors, Detectors, Electron., Signal Process.*, Nov. 1991, pp. 100–110.
[42] O. Ronneberger, P. Fischer, and T. Brox, "U-net: Convolutional networks for biomedical image segmentation," in *Proc. Int. Conf. Med. Image Comput. Comput.-Assist. Intervent.*, 2015, pp. 234–241.
[43] K. Liang, H. Yang, and Y. Xing, "Comparison of projection domain, image domain, and comprehensive deep learning for sparse-view X-ray CT image reconstruction," 2018, *arXiv:1804.04289*. [Online]. Available: http://arxiv.org/abs/1804.04289
[44] Y. Kim, J. Baek, and D. Hwang, "Ring artifact correction using detector line-ratios in computed tomography," *Opt. Express*, vol. 22, no. 11, pp. 13380–13392, May 2014.

WEI FANG received the B.S. degree from Tsinghua University, Beijing, China, in 2017, where he is currently pursuing the Ph.D. degree. His current research interests include dual/spectral CT reconstruction and deep learning.

LIANG LI (Senior Member, IEEE) received the B.S. and Ph.D. degrees from Tsinghua University, Beijing, China, in 2002 and 2007, respectively. He is currently an Associate Professor with the Department of Engineering Physics, Tsinghua University. He has authored 130 peer-reviewed journals and conference papers. His research interest includes the mathematical and physical problems of X-ray imaging and its security, industrial, medical, and other applications, especially the reconstruction problems under the special imaging conditions.

ZHIQIANG CHEN received the Ph.D. degree in engineering physics from Tsinghua University, Beijing, China, in 1999. He is currently a Professor with the Department of Engineering Physics, Tsinghua University. His research interests include X-ray imaging, computed tomography, image processing, and reconstruction.